inorganics

MDPI

Article

TiO_2-La_2O_3 as Photocatalysts in the Degradation of Naproxen

Adriana Marizcal-Barba [1], Isaias Limón-Rocha [1], Arturo Barrera [2], José Eduardo Casillas [2], O. A. González-Vargas [3], José Luis Rico [4], Claudia Martinez-Gómez [5] and Alejandro Pérez-Larios [1,*]

[1] Materials, Water and Energy Research Laboratory, Department of Engineering, Los Altos University Center, University of Guadalajara, Tepatitlán de Morelos 47600, Mexico; adriana.marizcal7736@alumnos.udg.mx (A.M.-B.); isaias.limon@cualtos.udg.mx (I.L.-R.)
[2] Laboratory of Catalytic Nanomaterials, Department of Basic Sciences, La Ciénega University Center, University of Guadalajara, Ocotlán 47820, Mexico; arturobr2003@yahoo.com.mx (A.B.) eduardo.casillas@cuci.udg.mx (J.E.C.)
[3] Control and Automation Engineering Department, School of Mechanical and Electrical Engineering-Zacatenco, National Polytechnic Institute, Ciudad de México 07738, Mexico; ogonzalezv@ipn.mx
[4] Catalysis Laboratory, Faculty of Chemical Engineering, Michoacan University of San Nicolás de Hidalgo, Morelia 58060, Mexico; jose.rico@umich.mx
[5] Department of Chemistry, Division of Natural and Exact Sciences, Campus Guanajuato, University of Guanajuato. Noria Alta S/N, Col. Noria Alta, Guanajuato 36050, Mexico; claudia.martinez@ugto.mx
* Correspondence: alarios@cualtos.udg.mx

Abstract: The indiscriminate use of naproxen as an anti-inflammatory has been the leading cause of pollution in sewage effluents. Conversely, titanium dioxide is one of the most promising photocatalyst for the degradation of pollutants. Ti-La mixed oxides containing 0, 1, 3, 5, and 10 wt.% of lanthanum were synthetized by sol-gel and tested as photocatalysts in the degradation of naproxen (NPX). The materials were further characterized by X-ray diffraction (XRD), nitrogen physisorption (BET), scanning electron microscopy (SEM), UV-Vis and Fourier-transform infrared spectroscopy (FT-IR), transmission electron microscopy (TEM), and X-ray photoelectron spectroscopy (XPS). The XRD patterns resembled that of anatase titania. The Eg values, determined from the UV-Vis spectra, vary from 2.07 to 3.2 eV corresponded to pure titania. The photocatalytic activity of these materials showed a degradation of naproxen from 93.6 to 99.8 wt.% after 4 h under UV irradiation.

Keywords: Naproxen; Degradation; Ti-La mixed oxides; Photocatalytic activity

Citation: Marizcal-Barba, A.; Limón-Rocha, I.; Barrera. A.; Casillas, J.E.; González-Vargas, O.A.; Rico, J.L.; Martinez-Gómez, C.; Pérez-Larios, A. TiO_2-La_2O_3 as Photocatalysts in the Degradation of Naproxen. *Inorganics* **2022**, *10*, 67. https://doi.org/10.3390/inorganics10050067

Academic Editor: Antonino Gulino

Received: 9 April 2022
Accepted: 19 May 2022
Published: 22 May 2022

1. Introduction

Drugs top the list of emerging contaminants detected in wastewater effluents [1]. The constant increase and chemical stability of these drugs hinders their removal and/or disposal in conventional wastewater treatment plants [2,3], which causes a deterioration of aquatic life [4,5]. Different water treatments have been reported using advanced oxidation processes (AOPs) [6–8] for the elimination of these drugs, such as anti-inflammatories [4,9], antipyretics, and analgesics [10,11]. Among the promising AOPs, photocatalysis stands out, since it manages to degrade and mineralize up to 100% of the contaminants [12,13]. Photocatalytic processes are based on the use of nanomaterials that have the ability to transfer charge between the semiconductor and the aqueous solution, of transference, where the redistribution caused by the absorption of photons ($h\nu$) generates the hollow electron pair (e^--h). This, when interacting in the medium, generates hydroxyl radicals (OH) and/or superoxide anions that can function as reducing or oxidizing agents to degrade organic molecules [14,15]. Among the most used photocatalysts are oxides such as TiO_2 [16], ZnO [17,18], Nb_2O_5 [19], CdS [20], and SnO_2 [21], among others [22]; some researchers have even used mixed oxides as nanocomposites to have greater efficiency in

the degradation of this type of contaminant, including TiO-ZnO [2,23], TiO_2-Fe_2O_3 [24], TiO-Al_2O_3 [25], Ti-Si-Fe [13], and Ti-Zr [26].

Many studies have focused on using TiO_2 either as a mixed oxide or as support because its use prevents the recombination of the photo- generated hollow electron pair (e^--h) and, thus, reduces the energy band [27–29]. Among the nanomaterials used for band gap reduction, rare earths can be found [30,31], such as Ce [32] and La [33]. The use of TiO_2-CeO in the degradation of dyes, lignin [34], and metronidazole [35] has been reported. TiO_2-La_2O_3 has been used to degrade volatile organic compounds [28], dyes [36–38], and drugs [39], and various catalysts have been reported to degrade mostly dyes (Table 1).

The effect of the synthesis parameters on the photocatalytic activity of Ti-La materials in the degradation of naproxen (NPX) is herein reported. Lanthanum is used as a dopant of titania for this purpose. The effect of La concentration on the photocatalytic activity is also explored. The samples are labelled as Ti-LaX where X represents the weight percentage of lanthanum.

Table 1. Titania-based nanocomposites with rare earths and their photocatalytic activity.

Catalyst	Contaminant	Type of Light	Reaction Time (min)	Efficiency	Reference
Ti-La	Methylene blue	UV irradiation	20	20%	[28]
Ti-Ce	Methylene blue	585 nm	20	<10%	[28]
Ti-Gd	Methylene blue	UV irradiation	20	20%	[28]
Ti-Ce	Metronidazole	Visible light illumination	120	50%	[35]
Ti-Ce/N/C	Metronidazole	Visible light illumination	120	100%	[35]
Ti-Co/Ce/La/Eu/Sm	Methylene blue	440–550 nm	30	>90%	[40]
TiO_2	Methylene blue	440–550 nm	30	<50%	[40]
Ti-Nd	Methyl orange	Simulated solar radiation (SSR)	240	>90%	[41]
Ti-Eu	Methyl orange	SSR	240	<70%	[41]
Ti-Tb	Methyl orange	SSR	240	<40%	[41]
TiO_2	Methyl orange	SSR	240	<50%	[41]
Ti-La	Methylene blue	484 nm	120	<70%	[42]
Ti-La/Tb	Methylene blue	484 nm	120	80%	[42]
Ti-Eu	Methyl orange	Simulated sunlight radiation	20	>95%	[34]
P25 TiO_2	Methyl orange	Simulated sunlight radiation	20	<50%	[34]
Ti-Sm	Lignin	Simulated sunlight radiation	90	>95%	[34]
P25 TiO_2	Lignin	Simulated sunlight radiation	90	<80%	[34]

Ti-La	Azo-dye acid orange 7	>420 nm	300	<80%	[43]
Ti-La-B	Azo-dye acid orange 7	>420 nm	300	>90%	[43]
Ti-Si-La	Methylene blue	UV irradiation	120	94%	[44]
TiO_2	Methylene blue	UV irradiation	120	<60%	[44]
Ti/bc-La	Methyl orange	UV irradiation	300	>85%	[37]
Ti/bc-Ce	Methyl orange	UV irradiation	300	>95%	[37]
Ti/bc	Methyl orange	UV irradiation	300	<60%	[37]
C,N,S-TiO_2	Ibuprofen	Visible light	300	>99%	[45]

2. Results and Discussion

2.1. Characterization.

2.1.1. Scanning Electron Microscopy

SEM micrographs of the Ti-La oxides after calcination are presented in Figure 1. Independent of the La content, the morphology of all samples is similar [28]. Agglomerates comprised of particles of about 200 nm are noticed in all samples. The elemental composition determined by Energy-dispersive X-ray spectroscopy (EDS) is also included in Figure 1. The calculated atomic ratios are consistent with the XPS results, in agreement with other research works [38,40].

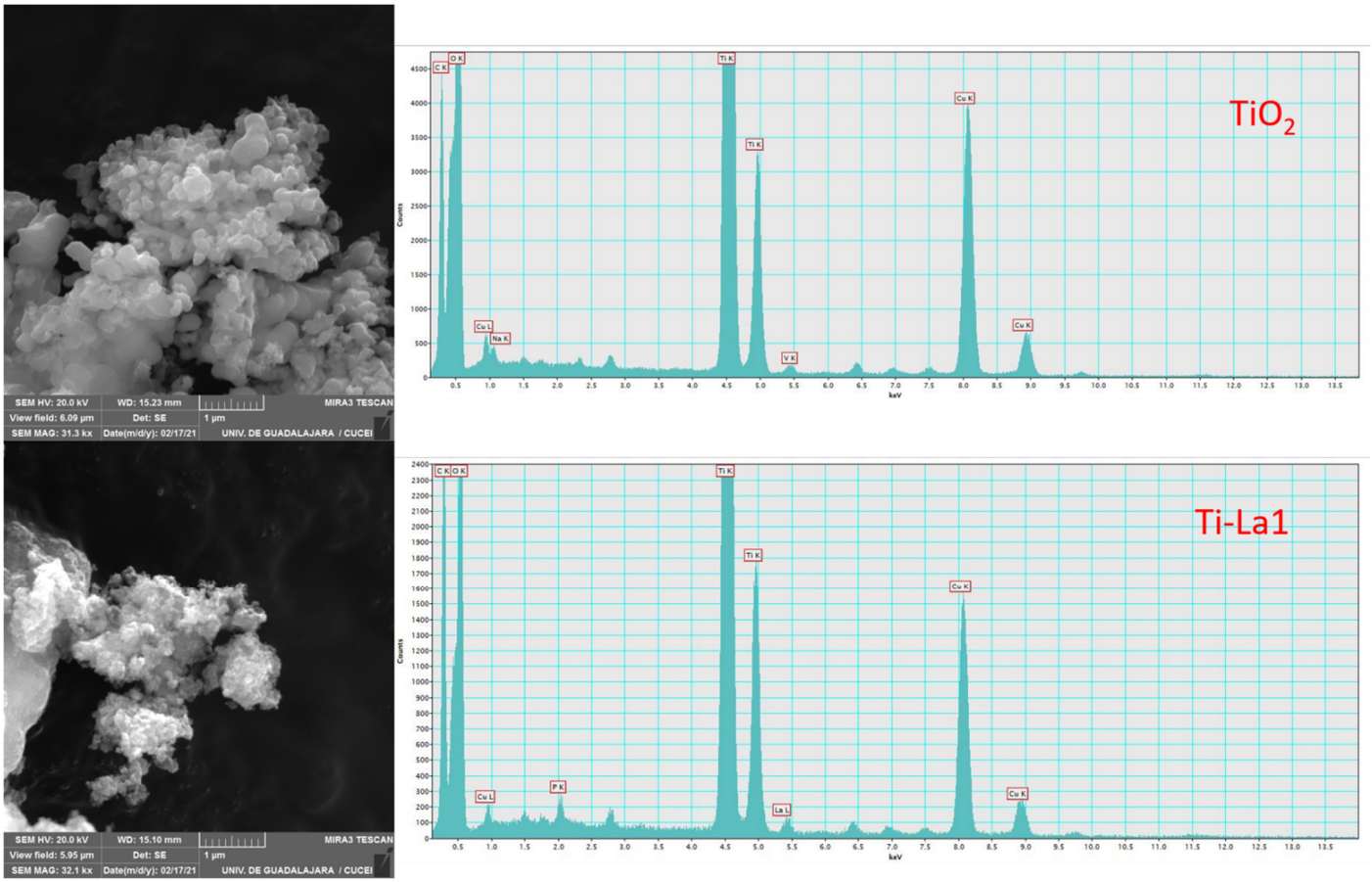

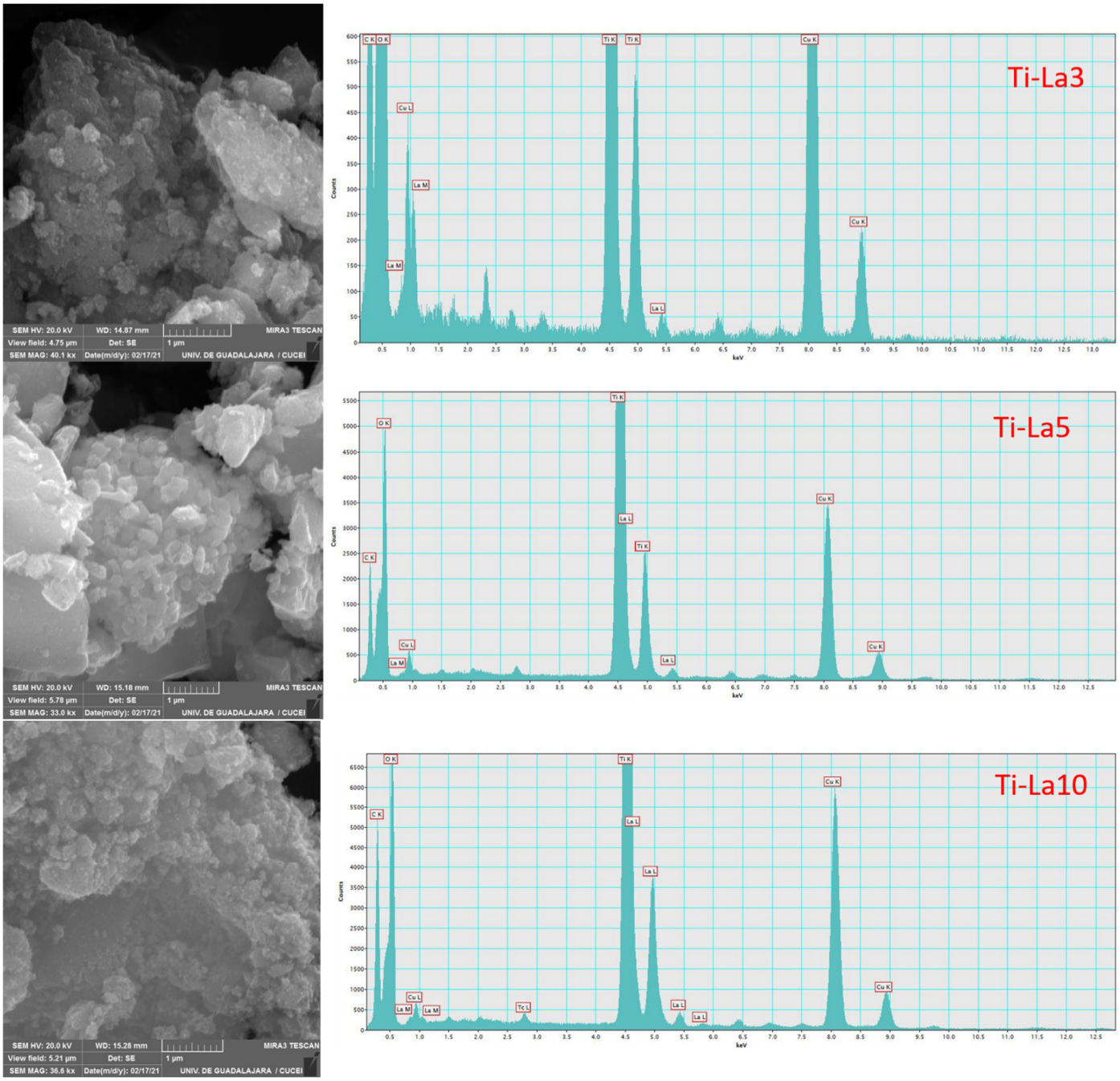

Figure 1. SEM micrographs and EDS spectra of the Ti-La nanocomposites.

2.1.2. Nitrogen Physisorption

Figure 2 shows the N_2 adsorption–desorption isotherms and the pore size distribution of the Ti-La samples. The isotherms are of type IV and present type H2 hysteresis associated with capillary condensation, Figure 2a. These isotherms are characteristic of mesopore materials [29]. Similar observations were previously noticed by Perez-Larios et al. for TiO_2-ZnO, Mn/TiO_2, Ti-Zr, and Ti-Co catalysts [20,24,30,31]. Figure 2b show unimodal pore distribution with a mean pore size which decreases as the lanthanum content augments. Table 2 presents the specific surface areas determined by the BET equation and the mean pore size of Ti-La samples. The presence of lanthanum into TiO_2 increases the specific surface areas proportionally, whereas the mean pore size increases for Ti-La1 compared to that for TiO_2 and then decreases as the lanthanum content augments.

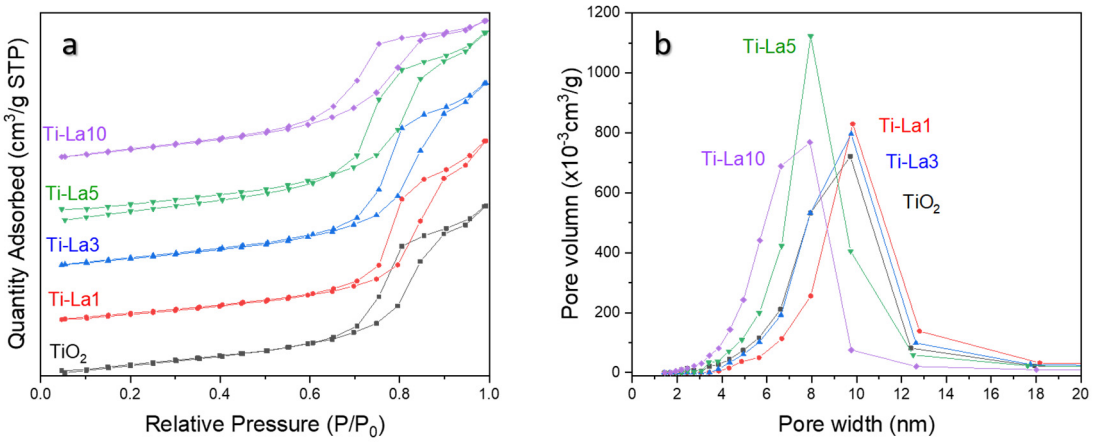

Figure 2. N_2 isotherms and pore size distribution of Ti-La samples.

2.1.3. X-ray Diffraction

The diffraction patterns of the calcined samples before the photocatalytic test are shown in Figure 3. All samples present diffractions which resemble those assigned for anatasa titania. The characteristic diffractions of anatase titania are located at 25, 37, 48, 54, 55, 62, 71, and 75 2θ degrees, which correspond to (101), (004), (200), (105), (211), (204), (116), and (311) crystallographic planes, respectively, according to JCPDS charts No. 00-001-0562 [9]. Additional peaks assigned to La_2O_3 were unnoticed, indicating, as a consequence, a well lanthanum distribution in the titanium oxide structure and/or the presence of small lanthanum oxides species out of the detection limit of the instrument. The most intensive diffraction at about 25.4 degrees 2θ decreases and became broader as the lanthanum content augments [45,46]. The unit cell parameters presented in Table 2 increase as the lanthanum content augments compared to that of pure titania. Furthermore, the crystallite size, D, decreases as function of lanthanum. Our results, therefore, suggest that La^{3+} cations are well dispersed in the titanium oxide structure, probably located in the interstitial positions since the ionic radii of La^{3+} is greater to that of Ti^{4+}, 0.106 and 0.062 nm, respectively [47], and substitution of titanium by lanthanum ions in the TiO_2 lattice is nonviable. However, assuming the presence of very small lanthanum oxides species (out of the detection limit of the XRD equipment) the replacement of lanthanum by titanium in the structure of lanthanum oxides is possible and Ti^{3+} can be formed [48,49]. The average crystallite sizes were determined using the Scherrer equation taken the half width (b) of the most intensive peak located at 25.4 degrees 2θ and are reported in Table 2. The average crystallite size of the Ti-La samples is significant reduced compared to that of pure titania (20.58 nm). Table 2 also shows that increasing the lanthanum content a further reduction in the average crystallite size is observed, as previously noticed for similar Ti-La samples [43,50,51].

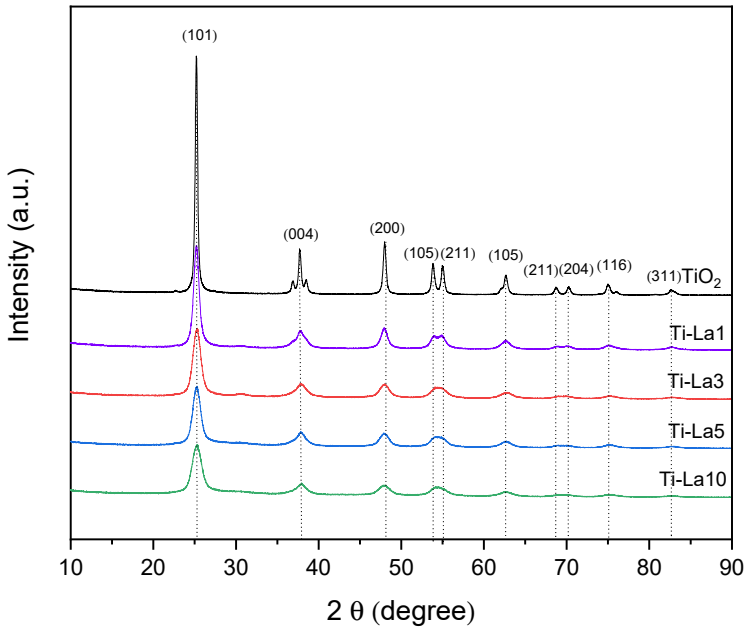

Figure 3. X-ray diffractograms of Ti-La nanocomposites.

Table 2. Physical and textural properties of Ti-La samples.

Samples	BET (m^2/g)	Pore Diameter (nm)	Cell Parameter a (Å)	Crystallite Size, D (nm)	E_g (eV)
Ti-La1	112.7	14.32	3.790	9.22	2.92
Ti-La3	127.8	12.95	3.792	6.52	2.99
Ti-La5	135.8	12.07	3.796	6.33	2.98
Ti-La10	144.6	8.99	3.820	5.21	3.01
TiO_2	64.0	6.5	3.790	20.58	3.05

2.1.4. UV-Vis Spectroscopy

Figure 4 shows the band gap energies of the Ti-La samples determined from UV-Vis spectra. The insert in this figure indicates that all samples exhibit an optical absorption at about 400 nm, which can be attributed to the electron transition of the Ti-O [52]. A slightly shift to the red region (2.92 to 3.01 eV) for the Ti-La samples compared to pure TiO_2 resulted after the incorporation of La^{3+} cations into TiO_2 lattice [41]. These observations are in agreement with other research works related to doped titania. A shift in the absorption edge to shorter wavenumber is clearly observed [53].

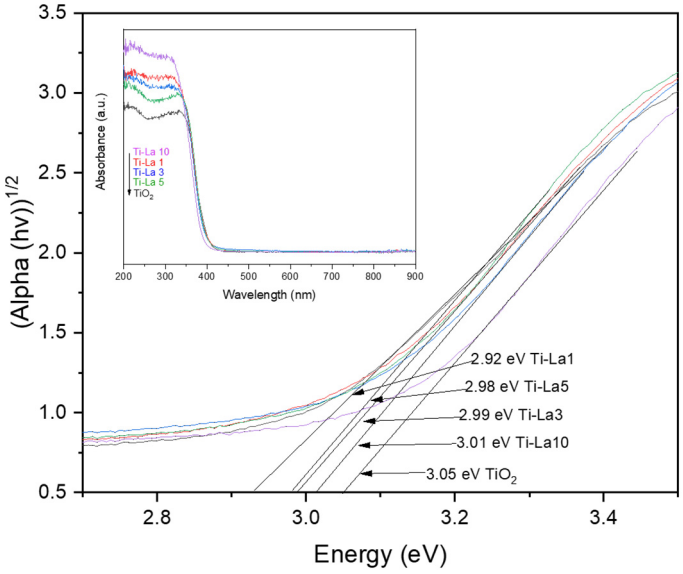

Figure 4. Band gap energies of the Ti-La samples determined from the UV-Vis spectra.

2.1.5. FT-IR Spectroscopy

Figure 5 shows the FTIR spectra of TiO_2 and Ti-La samples from 4000 to 400 cm^{-1}. The bands at about 448 cm^{-1} are associated to Ti-O vibrations [54] and related to the stretching of the Ti–OH and Ti–O bonds [38]. Although the samples were previously calcined before the FT-IR measurement, the bands at about 1600 and 1500 cm^{-1} correspond to C=O and C=C bonds originated from the residual organic compounds remained after synthesis [55].

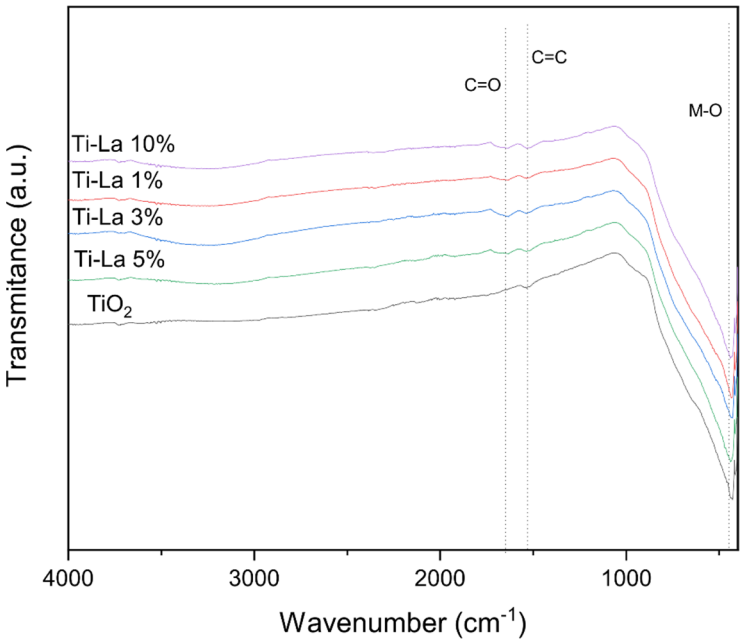

Figure 5. FT-IR spectra of TiO_2 and Ti-La nanocomposites.

2.1.6. X-Ray Photoelectron Spectrometry

The binding energies for Ti 2p are located at about 459 and 465 eV and correspond to Ti $2p_{3/2}$ and Ti $2p_{1/2}$, respectively. The separation of these two peaks is about 5.5 eV, which is in good agreement with previous publications related to doped titania (figure 6) [49,56,57].

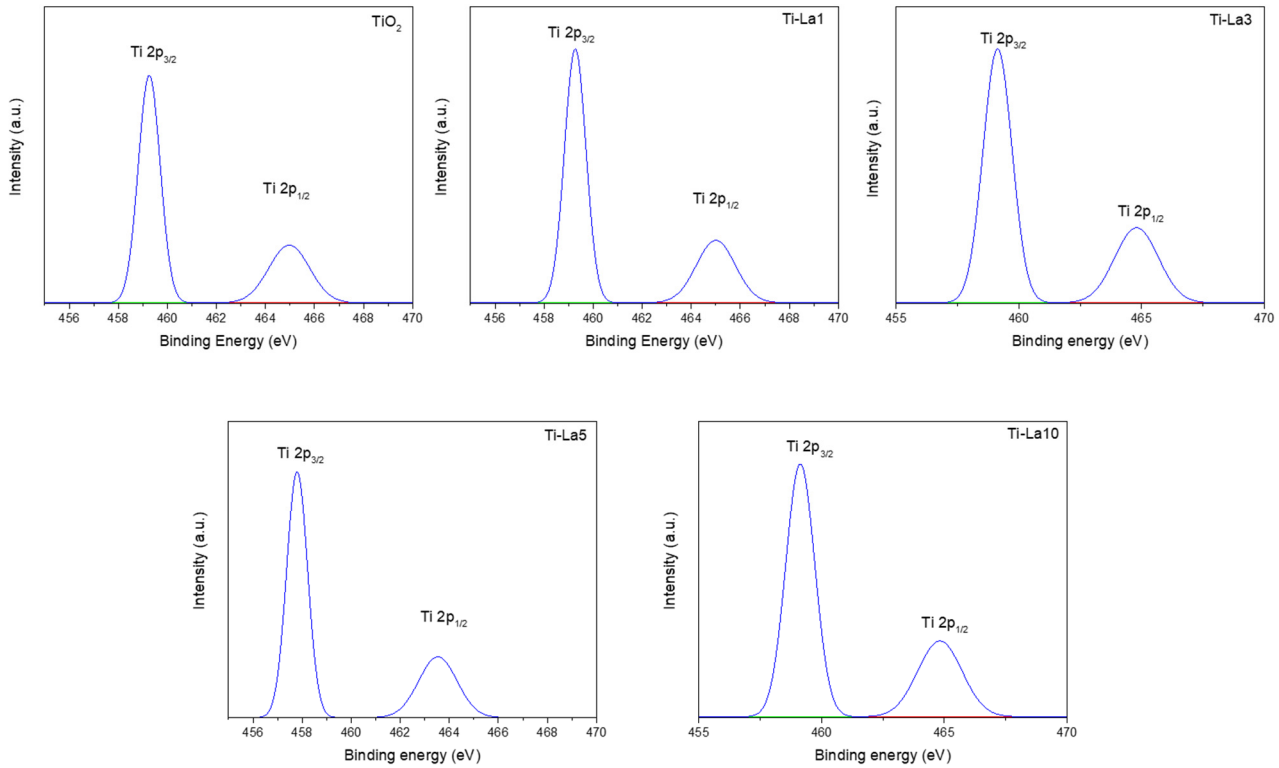

Figure 6. XPS spectra for Ti 2p.

The La $3d_{5/2}$ spectrum presents two peaks, one at about 834 eV and a satellite peak at about 839 eV, with a splitting of about 5 eV (Figure 7). Although the interpretation of the XPS spectrum of pure lanthanum oxide is complicated, since La is very sensitive to water and CO_2 from air and form a hydroxide and/or carbonate, it is likely that lanthanum as a dopant in our Ti-La samples is chemically more stable, since it is mainly buried into the titanium oxide structure. For a pure La_2O_3 sample exposed to air at ambient temperature, on which the formation of a hydroxide and/or carbonate have already occurred, the splitting of the two peaks of the La $3d_{5/2}$ spectrum is about 3.6 eV [57-60], whereas in ours, the separation is about 5 eV. The spectrum of the La $3d_{3/2}$ also shows two peaks, one about 851 eV and a satellite at about 856 eV. Their positions randomly change as function of the lanthanum content, similarly as those for La $3d_{5/2}$.

The XPS spectra for O 1s of the Ti-La samples are shown in Figure 8. Although oxygen is bound to titanium and lanthanum, its contribution is overlapped, since only one broad peak is present in all spectra. However, accordingly to the difference in electronegativity of both elements, the signal of the oxygen attached to titanium would appear at lower binding energy, compared to that of the oxygen bound to lanthanum [61]. The O 1s spectrum could be deconvoluted in two signals, an intense peak at about 530.5 eV and the other at about 532 eV, for the oxygen bound to titanium and lanthanum, respectively. The small peak at 532 eV would be in agreement with the low lanthanum content in the Ti-La samples [62].

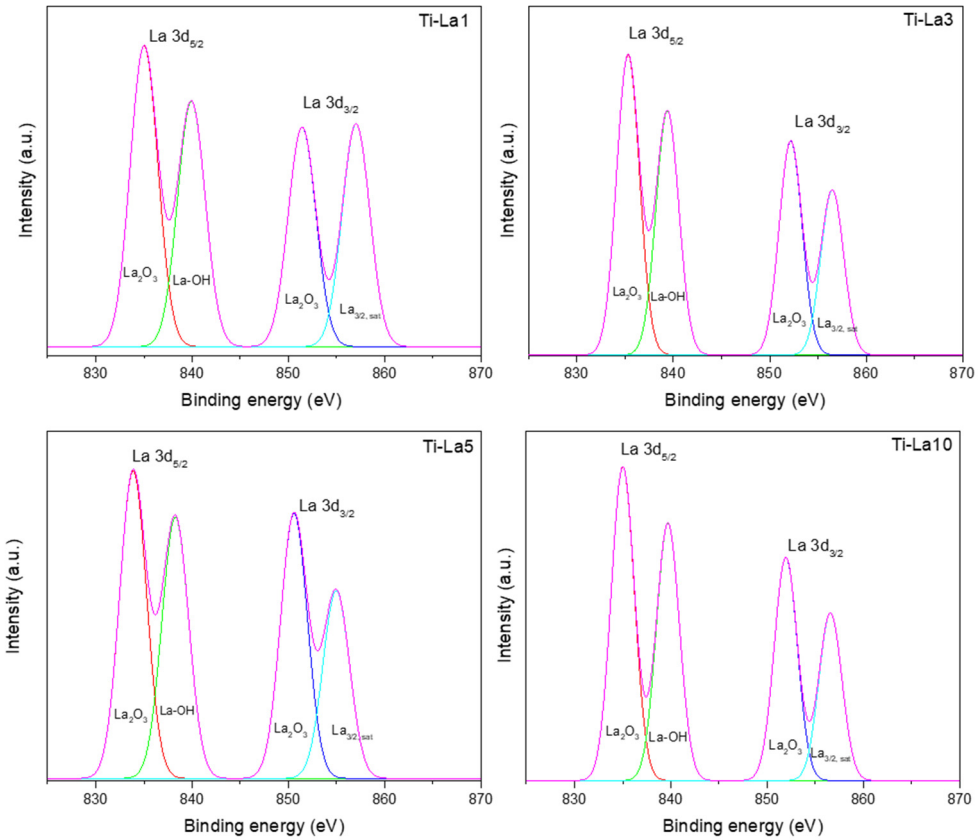

Figure 7. XPS spectra for La 3d.

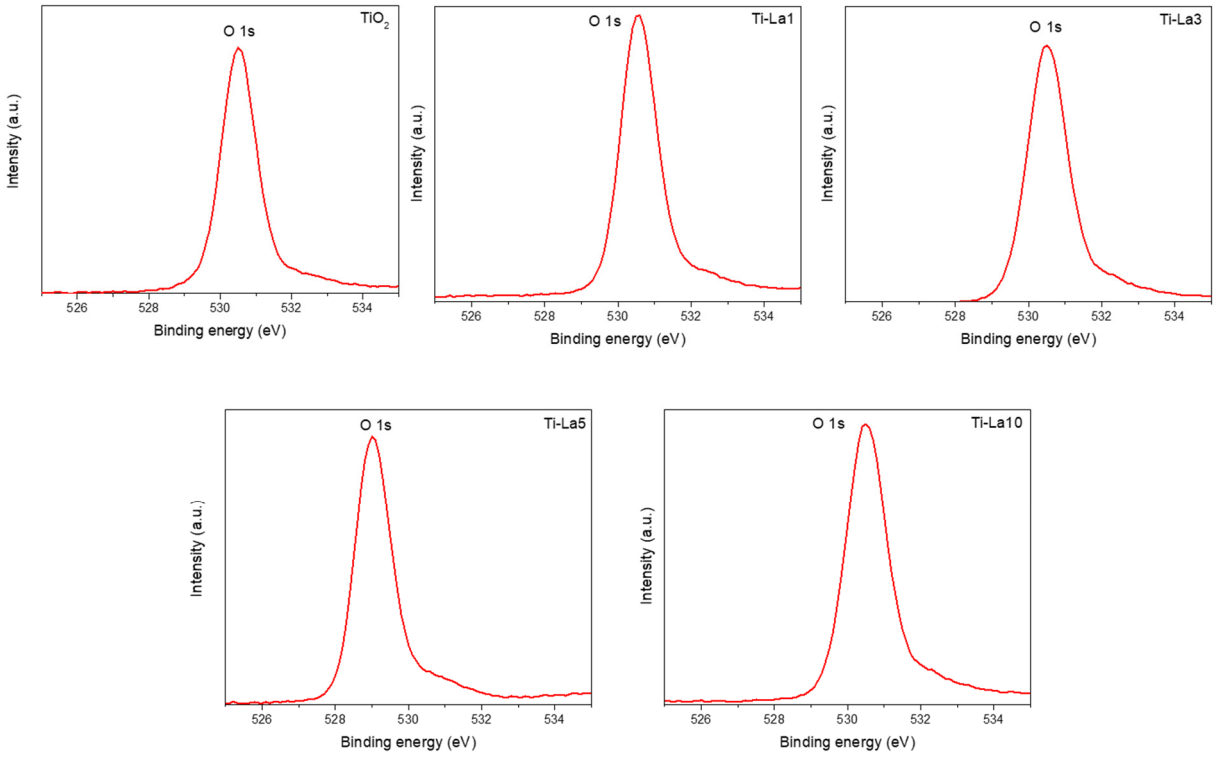

Figure 8. XPS spectra for O1s.

The presence of C in the XPS spectra, most likely resulting from the organic compounds used during synthesis, are presented in Figure 9. The C 1s spectra show a single broad peak at about 285 eV. However, their positions randomly change accordingly to the lanthanum content. It was reported that for a pure La_2O_3 sample exposed to air, the C 1s spectrum shows two signals, one at 284.5 and the other at 289.5 eV, assigned to adventitious carbon C 1s and to carbonate C 1s, respectively [63,64]. Since our C 1s spectra present a single broad peak centered at about 285 eV, the formation of lanthanum carbonate after exposing our Ti-La samples to air was excluded. Carbon species which remain after calcination, such as C-O-C and C=O, could well be present in our Ti-La samples.

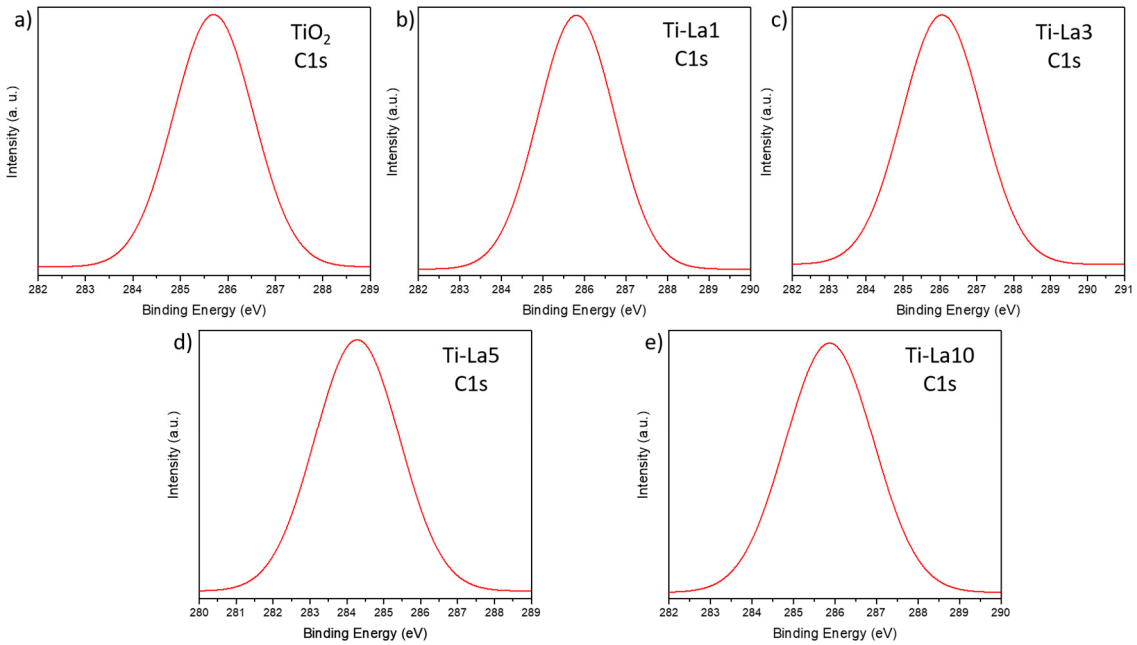

Figure 9. XPS spectra for C 1s.

Additional information obtained from XPS is presented in Table 3. The determined weight percentage is in agreement with the theoretical values. The shifts to lower binding energies for Ti-La5 in the Ti 2p and La 3d spectra, compared to other Ti-La samples, are unclear and more studies are required to elucidate these changes [57,60].

Table 3. Surface chemical states of Ti and La, and compositional analysis determined by XPS.

Element	Binding Energies in eV, and Chemical State				
	TiO_2	**Ti-La1**	**Ti-La3**	**Ti-La5**	**Ti-La10**
Ti $2p_{3/2}$	459.25	459.31	459.25	457.78	459.25
Chemical state	Ti^{4+}	Ti^{4+} + Ti^{3+}	Ti^{4+} + Ti^{3+}	Ti^{4+} + Ti^{3+}	Ti^{4+} + Ti^{3+}
Ti $2p_{1/2}$	464.96	464.99	464.73	463.53	464.76
Chemical state	Ti^{4+}	Ti^{4+} + Ti^{3+}	Ti^{4+} + Ti^{3+}	Ti^{4+} + Ti^{3+}	Ti^{4+} + Ti^{3+}
La $3d_{5/2}$	-	835.89	835.18	833.72	835.18
La $3d_{3/2}$	-	854.96	852.20	850.76	852.20
Chemical state	-	La^{3+}	La^{3+}	La^{3+}	La^{3+}
Weight% La	-	1.44	3.52	5.43	8.58

TEM images (Figure 10) show an interplanar spacing of 0.35 nm, corresponding to the (1 0 1) plane lattice space, typical of TiO_2 [40]. It can also be seen in nano-globular form with other nanostructures present for the Ti-La samples containing 1 3, 5, and 10 wt.% of

Lanthanum, respectively. The differences in contrast between the doped and pure titania confirm the incorporation of La^{3+} into the titania structure. The results are also consistent with those obtained from the XRD analysis and SEM.

Figure 10 presents some TEM images of the Ti and Ti-La samples before the photocatalytic test. The interplanar spacing of 0.35 nm, corresponding to the (1 0 1) plane of TiO_2 [40], changes as function of the lanthanum content which is in agreement with our XRD results. Further analysis of the TEM images to determine the nanoparticles size distribution was performed by the Imajej software measuring at least 50 nanoparticles [41–43].

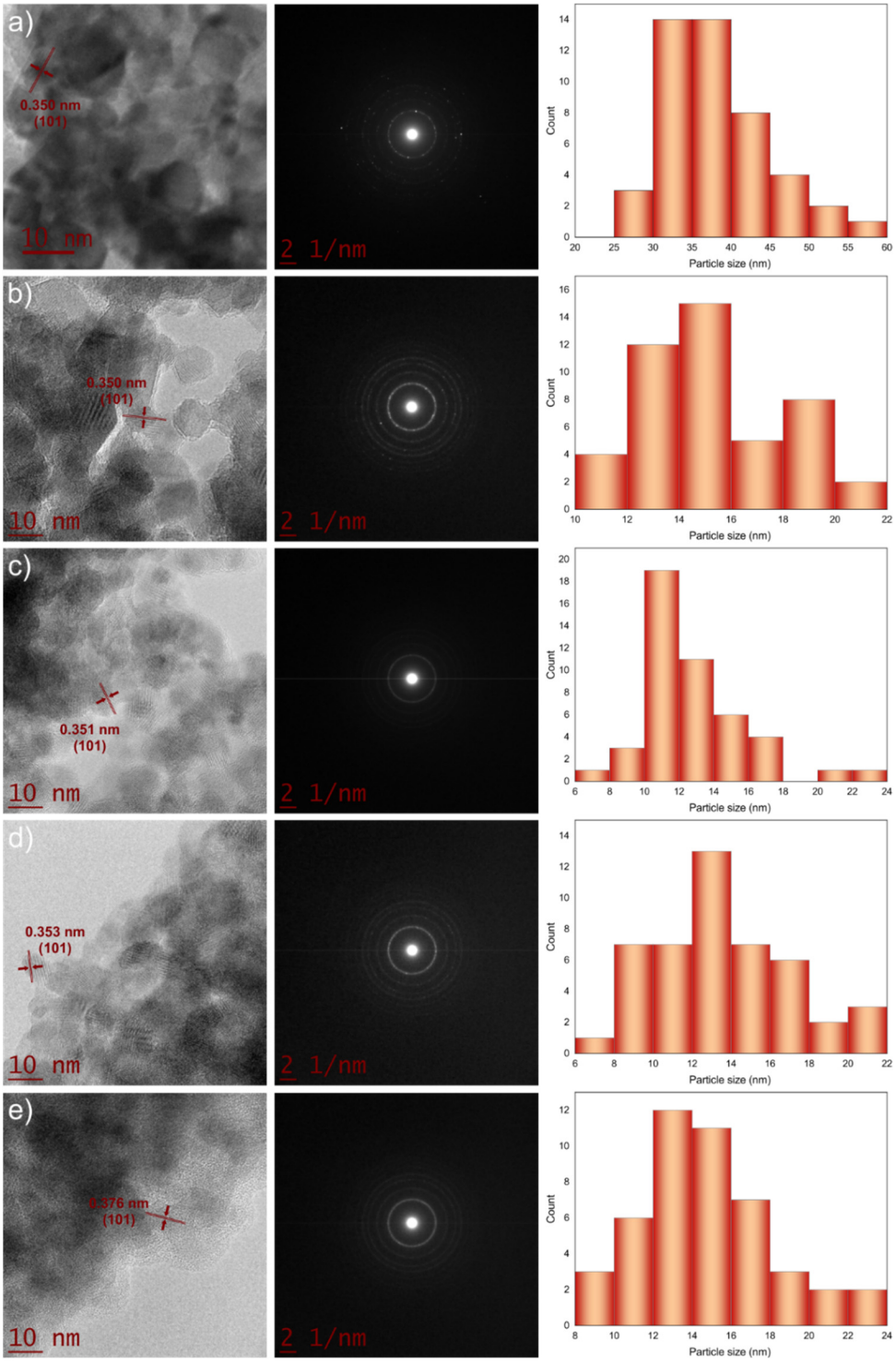

Figure 10. TEM images of photocatalysts, where (**a**) TiO_2, (**b**) Ti-La1, (**c**) Ti-La3, (**d**) Ti-La5, and (**e**) Ti-La10.

2.2. Phococatalytic Activity

Although the photocatalytic experiments were analyzed every 30 min, Figure 11 only shows the degradation of NPX from 120 min onwards. This was done to increase the visibility of the results at the end of the experiments. Among the samples, the best catalysts after 4 h under UV irradiation were Ti-La1, Degussa P25, and Ti-La3 which show more than 90% degradation of NPX. Conversely, in absence of a catalyst, the decomposition of NPX by photolysis using UV was about 30% after 4 h of reaction, results not shown.

Figure 11 shows the NPX photodegradation rate curves of the TiO_2, Ti-La1, Ti-La3, Ti-La5, and Ti-La10 nanophotocatalysts. The adsorption effect can be observed within the first 30 min, where the Ti-La nanocomposite adsorbs more contaminant than that of the bare TiO_2; this could be attributed to particle size and pore diameter, and these results are in agreement with previous reports where the Ti-Zr nanocomposite in the same relation at 1% degraded more than the others photocatalysts [56]. Otherwise, it is observed that the TiO_2, Ti-La1, and Ti-La3 samples turned out to be slightly more efficient than the Ti-La5 and Ti-La10 photocatalysts at 150 min. It is interesting to note that the Ti-La1 and Ti-La3 doping photocatalysts could lead to the formation of titania lattice distortion, which is prone to form the oxygen vacancy, and the vacancy could act as a trapper to inhibit the recombination of photo-generated electron-hole pairs [43]. It is a possibility that an impurity level has formed under the coactions of Ti^{3+} and oxygen vacancies by La doping, which could inhibit the recombination of charge carriers. Then, La_2O_3 on the TiO_2 surface could also transfer the electrons to the surface, which is advantageous for photocatalytic activity [42].

It can be seen from Figure 11, that pure TiO_2, (1×10^{-7} min^{-1}) showed a better photocatalytic activity than photolysis (9.7×10^{-6} min^{-1}) under UV light, indicating that nano-TiO_2 has an effect on accelerating the decomposition rate of NPX under UV light illumination. The nanocomposites Ti-La1 under the same experimental conditions was higher, which reveals that samples are readily excited under light irradiation, and photogenerated holes accelerate the oxidation of NPX before recombination with electrons. This result is consistent with other research [2,43,65,66]. Obviously, on this occasion, the optimal reaction time is 4 h, and the photocatalytic activity (1.5×10^{-6} min^{-1}) was better than that of TiO_2.

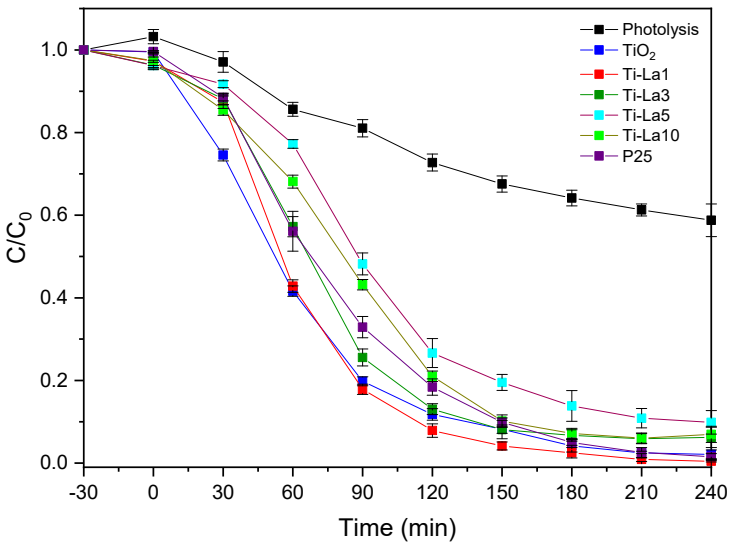

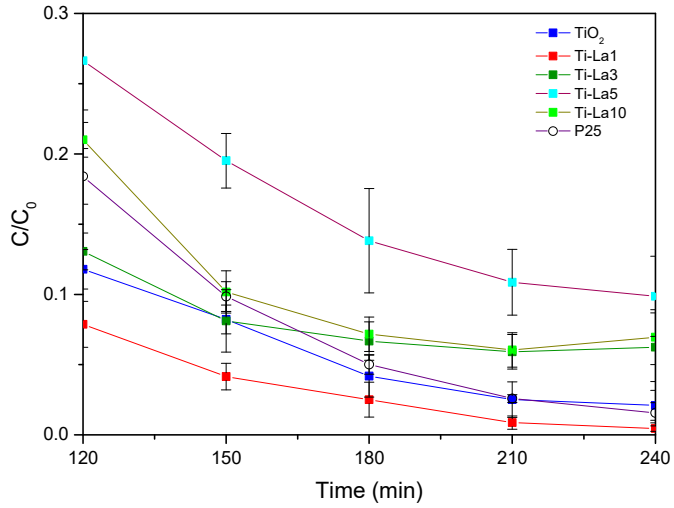

Figure 11. Naproxen degradation profiles in presence of TiO_2 or Ti-La photocatalysts under UV irradiation. Degussa P25 is used as a reference.

The reusability of TiO_2 and Ti-La samples was evaluated by repeating the NPX degradation five times using the same catalysts. After a run, the catalyst was separated by filtration and dried in an oven overnight. Each experiment was performed with a fresh NPX solution, using the spent catalyst, during 4 h and under UV irradiation. As it can be seen in Figure 12, the photocatalytic activity of Ti-La1 is still attractive, since it declined about 5% after the fifth run.

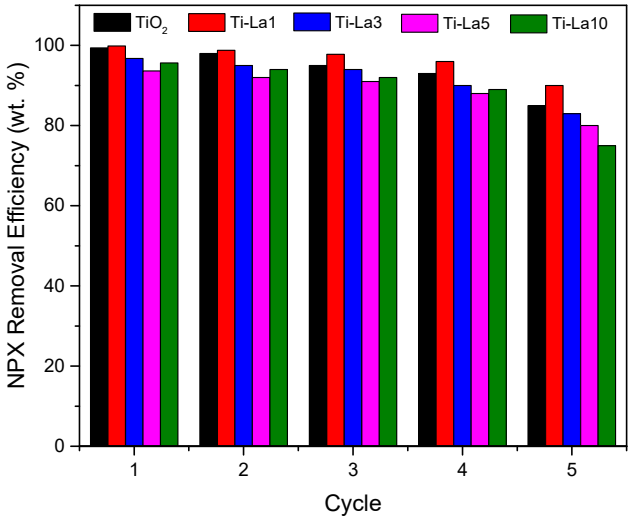

Figure 12. Recyclability of TiO_2 and Ti-La nanocomposites in the photocatalytic degradation of NPX under UV irradiation. The activities were determined after 4 h of reaction.

The total amount of carbon (TOC) found in the solutions after the photocatalytic tests were also determined and the percentages of mineralization are presented in Table 4. As can be seen, TiO_2 and Ti-La1 are not only effective in degrading but also to mineralize NPX. According to the literature, 2-acetyl-6-methoxynaphthalene, detected by HPLC, is the main intermediate during the decomposition of NPX [66].

Table 4. Decomposition and mineralization of NPX after 4 h in presence of catalysts and under UV.

Sample	% Degradation	Standard Deviation	% Mineralization	Standard Deviation
Ti-La1	99.55	±0.20	99.65	±0.08
Ti-La3	93.76	±0.24	93.78	±0.29
Ti-La5	90.13	±0.29	93.22	±0.47
Ti-La10	93.45	±0.29	94.45	±0.48
TiO_2	97.90	±0.19	99.64	±0.36
Photolysis	45.12	±0.39	18.92	±0.39

The mechanism for the activation of TiO_2 or Ti-La photocatalysts, under UV is similar to that previously reported by Chaker et al. for La/TiO_2 catalysts [27]. Briefly, the electrons and holes (e^- and h^+) generated during UV irradiation, reach the surface of the catalyst and react with water and oxygen to generate hydroxyl radicals and oxide radical anions through respective oxidative and reductive reactions. These radicals are strong oxidants and were able to decompose and mineralize NPX present in water. The differences in the photocatalytic activity of our samples are due to the physico-chemical properties of the catalysts. The following table summarizes the results presented in the literature concerning the decomposition of NPX on various catalysts. Although the information included in Table 5 is useful, comparison of the catalytic activities is not straightforward since the experimental conditions used in each research work were different.

Table 5. Degradation of NPX by heterogeneous photocatalysts.

Photocatalyst	Pharmaceutical Compound	Type of Irradiation	Reaction Time (min)	% Degradation	Reference
H_2O_2 modified titanate nanomaterial	Naproxen	Visible light	180	99.9	[67]
$BiVO_4$	Naproxen	Visible light	300	80%	[68]
AgBr-α-$NiMoO_4$	Naproxen	Visible light	20	84	[29]
TiO_2	Naproxen	Xe-lamp	180	40	[69]
SnO_2/AC	Naproxen	Direct sunlight	120	94	[70]
P25-TiO_2	Naproxen	Visible light	600	94	[71]

3. Conclusion

In summary, TiO_2 and Ti-La oxides were synthesized by sol-gel and tested as photocatalysts in the degradation of naproxen. Results from characterization indicate that the incorporation of lanthanum into titanium oxide increases the specific surface area and reduces the average crystalline size compared to those of pure TiO_2. In addition, lanthanum atoms are well distributed into the titanium oxide structure, probably located in the interstitial voids of the titania lattice. XPS results show that it is unlikely that lanthanum forms carbonate and/or a hydroxide after exposing our catalysts to air, since lanthanum atoms are well buried into the titanium oxide structure. XPS also shows that carbon species remain on the catalysts even after calcination. The photocatalytic activities of our samples in the degradation of NPX vary as function of the catalyst composition. Our results indicate that low concentration of lanthanum in titanium oxide is very attractive, since Ti-La1 showed the highest photocatalytic activity per mass of catalyst after 4 h and under UV irradiation. Furthermore, it was able to mineralize NPX and presents good stability after five cycles. The positive photocatalytic effects of Ti-La1 are probably related to the decrement in the recombination of electron-hole pairs.

4. Materials and Methods

4.1. Materials

All reactants (reagent grade) were acquired from Sigma Aldrich (Chemical Co., St. Louis MO., USA.), such as Titanium (IV) butoxide ($C_{16}H_{36}O_4Ti$, ≥ 97%), lanthanum nitrate ($La(NO)_3.6H_2O$, ≥ 99.9%), ethanol (CH_3CH_2OH, ≥ 96%), and naproxen ($CH_3OC_{10}H_6CH(CH_3)CO_2H$, ≥ 98%); deionized water (H_2O) was used in all experiments.

4.2. Catalyst Preparation

The Ti–La samples were prepared by sol-gel and the required quantities of titanium (IV) butoxide and lanthanum nitrate to prepare the oxides containing 1.0, 3.0, 5.0 and 10.0 wt.% of La in titania were used. The metal compounds were dissolved in 44 mL of ethanol and 18 mL of deionized water under stirring and the pH of the solution was adjusted to 3 with an aqueous nitric-acid solution. The water/alkoxide molar ratio was 8. The solution was heated up to 70 °C and kept at this temperature for 24 h. The resulting solids were dried at 100 °C during 24 h. After this treatment, the samples were annealed at 500 °C during 4 h, applying a heating rate of 2 °C/min. Pure titania prepared following a similar procedure, and a commercial catalyst, Degussa P25, were used as references. The samples were then ready to be used as photocatalysts in the photocatalytic degradation of NPX.

4.3. Characterization Equipment

The surface morphology of the mixed oxides was analyzed using a scanning electron microscope (Tescan, MIRA 3LMU, Boston, MA, USA)) operated at 20 kV and provided with an Energy Dispersive Spectrometer (Bruker, QUANTAX, MA, USA), which was utilized to determine the superficial elemental composition.

The textural properties of the catalytic samples were determined from nitrogen adsorption-desorption experiments using a micromeritics TriStar II Plus equipment (Norcross, GA, USA). The samples were first degassed under vacuum at 200 °C for 3 h. Nitrogen adsorption isotherms were measured at liquid-nitrogen temperature (77 K), and N_2 pressures ranging from 10–6 to 1.0 P/P_0. The specific surface areas were calculated following the Brunauer-Emmett-Teller (BET) method and the pore size distribution was obtained according to the Barret-Joyner-Halenda (BJH) method, using the Equation (1):

$$\ln (p/p^0) = 2\gamma V_m/\mathrm{RT}(r_p - t_c) \quad (1)$$

where r_p is the pore radius and t_c the thickness of the adsorbed multilayer film, which is formed prior to pore condensation [61].

The diffraction patterns of the mixed oxides were recorded using an X-ray diffractometer equipped with Cu Kα radiation (λ = 0.154 nm). The diffraction intensities as a function of 2θ were measured between 10 and 90°, using a step of 0.02° and counting time of 0.2 s per step. Furthermore, the average particle crystalline size was determined by the Scherer Equation (2) using the most intense peak for each sample:

$$\mathrm{D} = \frac{\mathrm{K}\lambda}{\beta Cos\,(\theta)}, \quad (2)$$

where K is the shape factor (0.89), λ is the X-ray wavelength (0.154 nm), β is the peak broadening at half maximum, and θ is the Bragg angle. Additionally, interplanar spacing (d) can be calculated from the Bragg law Equation (3):

$$d\,(A) = \frac{n\lambda}{2\sin\theta} \quad (3)$$

The UV-Vis absorption spectra were obtained using a UV-Vis spectrophotometer (Shimadzu UV-2600, Tokio, Japan) coupled with an integration sphere for diffuse reflectance studies. The equipment was calibrated with barium sulfate $BaSO_4$ as a reference. The optical absorption was measured in the wavelength range of 190 to 900 nm. From the plot,

the band gap energy for each sample was calculated using the following empirical Equation (4):

$$E_g = \frac{hC}{\lambda} \quad (4)$$

where E_g is the band gap energy; h is Plank constant equal to 6.626×10^{-34} J/s; C is the velocity of light equal to 2.99 × 108 m/s; and λ is the detection wavelength.

The FTIR spectra of the materials were recorded with an FTIR (Shimadzu, IRTracer-100, Tokyo, Japan) spectrophotometer using attenuated total reflectance (ATR) with a diamond waveguide (XR model). A detector of fast recovery deuterated triglycine sulfate (DTGS) (standard) was used for the analysis. The spectra were recorded at room temperature, with 24 scans and 4 cm^{-1} of resolution and from 4000 cm^{-1} to 400 cm^{-1}.

The XPS spectra were collected using a SPEC Phoibos 150 provided with a monochromatic Al Ka X-ray source (1487 eV). The position of the O 1s peak at 531.0 eV was monitored for each sample to ensure that no binding energy shift occurred due to charging.

High resolution images were acquired using a high-resolution transmission electron microscope, HRTEM, (Jeol microscope, JEM-ARM200F, Boston, MA, USA.) operated at 200 kV. The resulting images were analyzed using Gatan Micrograph software v. 3.7.0. (Pleasanton, CA, USA).

4.4. Photocatalytic Activity

The reaction was carried out in a 350mL Pyrex reactor using an aqueous solution of 30 mg/L NPX. For the photocatalytic experiments, 200 mg of photocatalyst was used in each run. The NPX solution was irradiated with a 1 $mW*cm^{-2}$ ultraviolet lamp of 254 nm wavelength submerged in a quartz tube at pH 7 ± 0.15. In the first 30 min, the absorption capacity of the material was measured under dark conditions. Irradiation was immediately started and samples were taken every 30 min for 4 h. The analysis of the samples was carried out in a Shimadzu model 2600 UV-Vis spectrophotometer at a wavelength of the maximum absorbance for NPX at 230 nm [2]. To determine the reusability, the spent catalyst was recovered, dried, and calcined, before reusing it.

The NPX concentration was calculated from the corresponding maximum absorption wavelength. The absorbance was proportional to the Beer–Lambert law in the range of the studied NPX concentrations. The degradation percentages of the NPX were calculated by the following equation (Equation (5)):

$$Degradation\ \% = (\frac{C}{C_0})100 \quad (5)$$

where C_0 and C is the initial and the actual concentration of NPX, and corresponds to a change in the current concentration of the NPX relative to the initial value of C_0 over time. Furthermore, the photocatalytic experiments were carried out three times to verify its reproducibility.

Furthermore, the total organic carbon in the samples was measured using a TOC-LCSN equipment (Shimadzu, model), and calculated applying the Equation (6).

$$TOC = TC - IC \quad (6)$$

where *TOC* is the amount of total organic carbon (mg L^{-1}), *TC* is the amount of total carbon (mg L^{-1}), and *IC* inorganic carbon (mg L^{-1}) in aqueous solution.

The quantitative analysis of the reaction kinetics of the degradation of organic compounds can be obtained by fitting the experimental data using the Langmuir–Hinshelwood model and expressed by the following Equation (7):

$$r = -\frac{dc}{dt} = \frac{kKc}{1 + Kc} \quad (7)$$

where k is the rate constant, K the equilibrium constant, and c is the concentration of the organic pollutant. Nonetheless, Equation (1) can be simplified due to the low concentration of pollutant $Kc < 1$ to adapt to the form of a first-order apparent rate Equation (8):

$$ln\ \frac{C_0}{C} = K_{App}t \quad (8)$$

where k_{App} is the apparent pseudo-first-order rate constant (min^{-1}), C and C_0 are the final and initial organic compound concentrations (mg L^{-1}), and t is the reaction time (min).

Author Contributions: Writing—original draft preparation, A.M.-B.; writing—review and editing, C.M.-G., A.B., J.E.C., O.A.G.-V., I.L.-R., J.L.R. and A.P.-L.; All authors have read and agreed to the published version of the manuscript.

Funding: This research received no external funding.

Institutional Review Board Statement: "Not applicable"

Informed Consent Statement: "Not applicable"

Data Availability Statement: "Not applicable"

Acknowledgments: Marizcal-Barba thanks CONACYT for the scholarship (799894) and appreciates the support of the microscopy Lab for characterization of photocatalysts to Martín Flores and Milton Vázquez, as well as the technicians of the equipment Ing. Sergio Oliva and José Rivera, for the characterization by XRD, SEM-DES, and XPS analysis (project 270660, Support for the Strengthening and Development of the Scientific and Technological Infrastructure).

Conflicts of Interest: The authors declare no conflicts of interest.

Abbreviations

TiO_2	Titanium dioxide
NPX	naproxene
XRD	X-ray diffraction
SEM	scanning electron microscopy
EDS	Energy Dispersive X-Ray
UV-Vis	Visible and ultra-violet ligth
FT-IR	Fourier Transform Infrared Spectroscopy
TEM	transmission electron microscopy
XPS	X-ray photoelectron spectroscopy
AOP's	Advanced Oxidation Processes
OH	hydroxyl radicals
BET	Brunauer-Emmett-Teller
BJH	Barrett-Joyner-Halenda
JCPDS	Joint Committee on Powder Diffraction Standards
M-O	Metal-Oxygen
eV	electron Volt
TOC	Total Organic Carbon
TC	Total Carbon
IC	Inorganic Carbon
HPLC	High Performance Liquid Chromatography

References

1. Uheida, A.; Mohamed, A.; Belaqziz, M.; Nasser, W.S. Photocatalytic degradation of Ibuprofen, Naproxen, and Cetirizine using PAN-MWCNT nanofibers crosslinked TiO_2-NH_2 nanoparticles under visible light irradiation. *Sep. Purif. Technol.* **2019**, *212*, 110–118. https://doi.org/10.1016/j.seppur.2018.11.030.
2. Strbac, D.; Aggelopoulos, C.; Štrbac, G.; Dimitropoulos, M.; Novaković, M.; Ivetić, T.; Yannopoulos, S.N. Photocatalytic degradation of Naproxen and methylene blue: Comparison between ZnO, TiO_2 and their mixture. *Process Saf. Environ. Prot.* **2018**, *113*, 174–183. https://doi.org/10.1016/j.psep.2017.10.007.

3. Kaur, M., Mehta, S. K. and Kansal, S. K. Construction of Multifunctional NH_2-UiO-66 Metal Organic Framework: Sensing and Photocatalytic Degradation of Ketorolac Tromethamine and Tetracycline in Aqueous Medium. *Environmental Science and Pollution Research*, **2021**, 1-21.
4. Pylypchuk, I.V.; Daniel, G.; Kessler, V.G.; Seisenbaeva, G.A. Removal of Diclofenac, Paracetamol, and Carbamazepine from Model Aqueous Solutions by Magnetic Sol–Gel Encapsulated Horseradish Peroxidase and Lignin Peroxidase Composites. *Nanomaterials* **2020**, *10*, 282. https://doi.org/10.3390/nano10020282.
5. Wojcieszyńska, D.; Guzik, U. Naproxen in the environment: Its occurrence, toxicity to nontarget organisms and biodegradation. *Appl. Microbiol. Biotechnol.* **2020**, *104*, 1849–1857. https://doi.org/10.1007/s00253-019-10343-x.
6. Martínez-Huitle, C.A.; Panizza, M. Electrochemical oxidation of organic pollutants for wastewater treatment. *Curr. Opin. Electrochem.* **2018**, *11*, 62–71. https://doi.org/10.1016/j.coelec.2018.07.010.
7. Bello, M.M.; Raman, A.A.A.; Asghar, A. A review on approaches for addressing the limitations of Fenton oxidation for recalcitrant wastewater treatment. *Process Saf. Environ. Prot.* **2019**, *126*, 119–140. https://doi.org/10.1016/j.psep.2019.03.028.
8. Glaze, W.H. Reaction products of ozone: A review. *Environ. Health Perspect.* **1986**, *69*, 151–157. https://doi.org/10.1289/ehp.8669151.
9. Ahmadpour, N.; Sayadi, M.H.; Sobhani, S.; Hajiani, M. A potential natural solar light active photocatalyst using magnetic $ZnFe_2O_4$ @ TiO_2/Cu nanocomposite as a high performance and recyclable platform for degradation of naproxen from aqueous solution. *J. Clean. Prod.* **2020**, *268*, 122023. https://doi.org/10.1016/j.jclepro.2020.122023.
10. Mohamed, A.; Salama, A.; Nasser, W.S.; Uheida, A. Photodegradation of Ibuprofen, Cetirizine, and Naproxen by PAN-MWCNT/TiO_2–NH_2 nanofiber membrane under UV light irradiation. *Environ. Sci. Eur.* **2018**, *30*, 47. https://doi.org/10.1186/s12302-018-0177-6.
11. Castro-Pastrana, L.; Cerro-López, M.; Toledo-Wall, M.; Gómez-Oliván, L.; Saldívar-Santiago, M.; Castro-Pastrana, L.; Cerro-López, M.; Toledo-Wall, M.; Gómez-Oliván, L.; Saldívar-Santiago, M. Análisis de fármacos en aguas residuales de tres hospitales de la ciudad de Puebla, México. *Ing. Del Agua* **2021**, *25*, 59. https://doi.org/10.4995/ia.2021.13660.
12. Reyes, M.H.; Solis, R.C.; Ruiz, F.; Rodriguez-Gonzalez, V.; Moctezuma, E. Promotional effect of metal doping on nanostructured TiO2 during the photocatalytic degradation of 4-chlorophenol and naproxen sodium as pollutants. *Mater. Sci. Semicond. Process.* **2019**, *100*, 130–139. https://doi.org/10.1016/j.mssp.2019.04.050.
13. Amini, Z.; Givianrad, M.H.; Saber-Tehrani, M.; Azar, P.A.; Husain, S.W. Synthesis of N-doped TiO_2/SiO_2/Fe_3O_4 magnetic nanocomposites as a novel purple LED illumination-driven photocatalyst for photocatalytic and photoelectrocatalytic degradation of naproxen: Optimization and different scavenger agents study. *J. Environ. Sci. Health Part A* **2019**, *54*, 1254–1267. https://doi.org/10.1080/10934529.2019.1673609.
14. Marizcal-Barba, A.; Sanchez-Burgos, J.A.; Zamora-Gasga, V.; Larios, A.P. Study of the Response Surface in the Photocatalytic Degradation of Acetaminophen Using TiO_2. *Photochem* **2022**, *2*, 225–236. https://doi.org/10.3390/photochem2010017.
15. Eidsvåg, H.; Bentouba, S.; Vajeeston, P.; Yohi, S.; Velauthapillai, D. TiO_2 as a Photocatalyst for Water Splitting—An Experimental and Theoretical Review. *Molecules* **2021**, *26*, 1687. https://doi.org/10.3390/molecules26061687.
16. Abel, S.; Jule, L.T.; Belay, F.; Shanmugam, R.; Dwarampudi, L.P.; Nagaprasad, N.; Krishnaraj, R. Application of Titanium Dioxide Nanoparticles Synthesized by Sol-Gel Methods in Wastewater Treatment. *J. Nanomater.* **2021**, *2021*, 1–6. https://doi.org/10.1155/2021/3039761.
17. Primo, J.D.O.; Bittencourt, C.; Acosta, S.; Sierra-Castillo, A.; Colomer, J.-F.; Jaerger, S.; Teixeira, V.C.; Anaissi, F.J. Synthesis of Zinc Oxide Nanoparticles by Ecofriendly Routes: Adsorbent for Copper Removal from Wastewater. *Front. Chem.* **2020**, *8*, 571790. https://doi.org/10.3389/fchem.2020.571790.
18. Limón-Rocha, I.; Guzmán-González, C.A.; Anaya-Esparza, L.M.; Romero-Toledo, R.; Rico, J.L.; González-Vargas, O.A.; Pérez-Larios, A. Effect of the Precursor on the Synthesis of ZnO and Its Photocatalytic Activity. *Inorganics* **2022**, *10*, 16. https://doi.org/10.3390/inorganics10020016.
19. Troncoso, F.D.; Tonetto, G.M. Nb2O5 monolith as an efficient and reusable catalyst for textile wastewater treatment. *Sustain. Environ. Res.* **2021**, *31*, 35. https://doi.org/10.1186/s42834-021-00109-4.
20. Al-Enizi, A.M.; El-Halwany, M.M.; Al-Abdrabalnabi, M.A.; Bakrey, M.; Ubaidullah, M.; Yousef, A. Novel Low Temperature Route to Produce CdS/ZnO Composite Nanofibers as Effective Photocatalysts. *Catalysts* **2020**, *10*, 417. https://doi.org/10.3390/catal10040417.
21. Sakwises, L.; Pisitsak, P.; Manuspiya, H.; Ummartyotin, S. Effect of Mn-substituted SnO2 particle toward photocatalytic degradation of methylene blue dye. *Results Phys.* **2017**, *7*, 1751–1759. https://doi.org/10.1016/j.rinp.2017.05.009.
22. Qin, Y.; Fang, F.; Xie, Z.; Lin, H.; Zhang, K.; Yu, X.; Chang, K. La,Al-Codoped $SrTiO_3$ as a Photocatalyst in Overall Water Splitting: Significant Surface Engineering Effects on Defect Engineering. *ACS Catal.* **2021**, *11*, 11429–11439. https://doi.org/10.1021/acscatal.1c02874.
23. Mousa, H.M.; Alenezi, J.F.; Mohamed, I.M.; Yasin, A.S.; Hashem, A.-F.M.; Abdal-Hay, A. Synthesis of TiO2@ZnO heterojunction for dye photodegradation and wastewater treatment. *J. Alloy. Compd.* **2021**, *886*, 161169. https://doi.org/10.1016/j.jallcom.2021.161169.
24. Ameur, N.; Bachir, R.; Bedrane, S.; Choukchou-Braham, A. A Green Route to Produce Adipic Acid on TiO_2-Fe_2O_3 Nanocomposites. *J. Chin. Chem. Soc.* **2017**, *64*, 1096–1103. https://doi.org/10.1002/jccs.201700130.

25. Ahmad, R.; Kim, J.K.; Kim, J.H.; Kim, J. Effect of polymer template on structure and membrane fouling of TiO_2 /Al_2O_3 composite membranes for wastewater treatment. *J. Ind. Eng. Chem.* **2018**, *57*, 55–63. https://doi.org/10.1016/j.jiec.2017.08.007.
26. Pérez-Larios, A.; Rico, J.L.; Anaya-Esparza, L.M.; Vargas, O.G.; González-Silva, N.; Gómez, R. Hydrogen Production from Aqueous Methanol Solutions Using Ti–Zr Mixed Oxides as Photocatalysts under UV Irradiation. *Catalysts* **2019**, *9*, 938. https://doi.org/10.3390/catal9110938.
27. Chaker, H.; Ameur, N.; Saidi-Bendahou, K.; Djennas, M.; Fourmentin, S. Modeling and Box-Behnken design optimization of photocatalytic parameters for efficient removal of dye by lanthanum-doped mesoporous TiO_2. *J. Environ. Chem. Eng.* **2021**, *9*, 104584. https://doi.org/10.1016/j.jece.2020.104584.
28. Rozman, N.; Tobaldi, D.M.; Cvelbar, U.; Puliyalil, H.; Labrincha, J.A.; Legat, A.; Škapin, A.S. Hydrothermal Synthesis of Rare-Earth Modified Titania: Influence on Phase Composition, Optical Properties, and Photocatalytic Activity. *Materials* **2019**, *12*, 713. https://doi.org/10.3390/ma12050713.
29. Ray, S.K.; Dhakal, D.; Lee, S.W. Rapid degradation of naproxen by AgBr-α-$NiMoO_4$ composite photocatalyst in visible light: Mechanism and pathways. *Chem. Eng. J.* **2018**, *347*, 836–848. https://doi.org/10.1016/j.cej.2018.04.165.
30. Weber, A.S.; Grady, A.M.; Koodali, R.T. Lanthanide modified semiconductor photocatalysts. *Catal. Sci. Technol.* **2012**, *2*, 683–693.
31. Baiju, K.; Sibu, C.; Rajesh, K.; Pillai, P.K.; Mukundan, P.; Warrier, K.; Wunderlich, W. An aqueous sol–gel route to synthesize nanosized lanthana-doped titania having an increased anatase phase stability for photocatalytic application. *Mater. Chem. Phys.* **2005**, *90*, 123–127. https://doi.org/10.1016/j.matchemphys.2004.10.024.
32. Štengl, V.; Bakardjieva, S.; Murafa, N. Preparation and photocatalytic activity of rare earth doped TiO_2 nanoparticles. *Mater. Chem. Phys.* **2009**, *114*, 217–226. https://doi.org/10.1016/j.matchemphys.2008.09.025.
33. Sibu, C.P.; Kumar, S.R.; Mukundan, P.; Warrier, K.G.K. Structural Modifications and Associated Properties of Lanthanum Oxide Doped Sol-Gel Nanosized Titanium Oxide. *Chem. Mater.* **2002**, *14*, 2876–2881. https://doi.org/10.1021/cm010966p.
34. Song, L.; Zhao, X.; Cao, L.; Moon, J.-W.; Gu, B.; Wang, W. Synthesis of rare earth doped TiO_2 nanorods as photocatalysts for lignin degradation. *Nanoscale* **2015**, *7*, 16695–16703. https://doi.org/10.1039/c5nr03537f.
35. Elgendy, K.; Elmehasseb, I.; Kandil, S. Synthesis and characterization of rare earth metal and non-metal co-doped TiO_2 nanostructure for photocatalytic degradation of Metronidazole. *Environment* **2019**, *2508*, 60–67.
36. Du, J.; Li, B.; Huang, J.; Zhang, W.; Peng, H.; Zou, J. Hydrophilic and photocatalytic performances of lanthanum doped titanium dioxide thin films. *J. Rare Earths* **2013**, *31*, 992–996. https://doi.org/10.1016/s1002-0721(13)60019-8.
37. Zhang, X.; Chen, W.; Lin, Z.; Yao, J.; Tan, S. Preparation and Photocatalysis Properties of Bacterial Cellulose/TiO_2 Composite Membrane Doped with Rare Earth Elements. *Synth. React. Inorganic Met. Nano-Metal Chem.* **2011**, *41*, 997–1004. https://doi.org/10.1080/15533174.2011.591334.
38. Liu, J.; Yang, R.; Li, S. Synthesis and Photocatalytic Activity of TiO_2/V_2O_5 Composite Catalyst Doped with Rare Earth Ions. *J. Rare Earths* **2007**, *25*, 173–178. https://doi.org/10.1016/s1002-0721(07)60068-4.
39. Zhu, L.; Xiao, Y.F.; Wang, X. The Photocatalytic Oxidation Properties of La^{3+}-Doped and Ce^{4+}-Doped ZnO-TiO_2 in Treating Pharmaceutical Wastewater. *Adv. Mater. Res.* **2013**, *726–731*, 2988–2992. https://doi.org/10.4028/www.scientific.net/amr.726-731.2988.
40. Li, S.; Yang, Y.; Su, Q.; Liu, X.; Zhao, H.; Zhao, Z.; Li, J.; Jin, C. Synthesis and photocatalytic activity of transition metal and rare earth element co-doped TiO2 nano particles. *Mater. Lett.* **2019**, *252*, 123–125. https://doi.org/10.1016/j.matlet.2019.05.123.
41. Đorđević, V.; Milićević, B.; Dramićanin, M.D. Rare Earth-Doped Anatase TiO_2 Nanoparticles. In *Titanium Dioxide*; InTech: London, UK, 2017.
42. Smitha, V.S.; Saju, P.; Hareesh, U.S.; Swapankumar, G.; Warrier, K.G.K. Optical Properties of Rare-Earth Doped TiO_2 Nanocomposites and Coatings; A Sol-Gel Strategy towards Multi-functionality. *ChemistrySelect* **2016**, *1*, 2140–2147. https://doi.org/10.1002/slct.201600606.
43. Lan, X.; Wang, L.; Zhang, B.; Tian, B.; Zhang, J. Preparation of lanthanum and boron co-doped TiO2 by modified sol–gel method and study their photocatalytic activity. *Catal. Today* **2014**, *224*, 163–170. https://doi.org/10.1016/j.cattod.2013.10.062.
44. Smitha, V.S.; Jyothi, C.K.; Mohamed A.P.; Pillai, S.; Warrier, K.G. Novel multifunctional titania–silica–lanthanum phosphate nanocomposite coatings through an all aqueous sol–gel process. *Dalton Trans.* **2013**, *42*, 4602–4612. https://doi.org/10.1039/c2dt32675b.
45. Khedr, T.M.; El-Sheikh, S.M.; Hakki, A.; Ismail, A.A.; Badawy, W.A.; Bahnemann, D.W. Highly active non-metals doped mixed-phase TiO 2 for photocatalytic oxidation of ibuprofen under visible light. *J. Photochem. Photobiol. A Chem.* **2017**, *346*, 530–540. https://doi.org/10.1016/j.jphotochem.2017.07.004.
46. Escudero, A.; Becerro, A.I.; Carrillo-Carrion, C.; Núñez, N.O.; Zyuzin, M.V.; Laguna, M.; González, D.; Ocaña, M.; Parak, W.J. Rare earth based nanostructured materials: Synthesis, functionalization, properties and bioimaging and biosensing applications. *Nanophotonics* **2017**, *6*, 881–921. https://doi.org/10.1515/nanoph-2017-0007.
47. Sing, K.S.W.; Everett, D.H.; Haul, R.A.W.; Moscou, L.; Pierotti, R.A.; Rouquerol, J.; Siemieniewska, T. Reporting Physisorption Data for Gas/Solid Systems with Special Reference to the Determination of Surface Area and Porosity. *Pure Appl. Chem.* **1985**, *57*, 603–619. https://doi.org/10.1351/PAC198557040603/MACHINEREADABLECITATION/RIS.

48. Pérez-Larios, A.; Hernández-Gordillo, A.; Morales-Mendoza, G.; Lartundo-Rojas, L.; Mantilla, Á.; Gómez, R. Enhancing the H_2 evolution from water–methanol solution using Mn^{2+}–Mn^{+3}–Mn^{4+} redox species of Mn-doped TiO_2 sol–gel photocatalysts. *Catal. Today* **2016**, *266*, 9–16. https://doi.org/10.1016/j.cattod.2015.12.029.
49. Pérez-Larios, A.; Torres-Ramos, I.; Zanella, R.; Rico, J.L. Ti-Co mixed oxide as photocatalysts in the generation of hydrogen from water. *Int. J. Chem. React. Eng.* **2022**, *20*, 129–140. https://doi.org/10.1515/ijcre-2021-0049.
50. Kabir, H.; Nandyala, S.H.; Rahman, M.M.; Kabir, M.A.; Stamboulis, A. Influence of calcination on the sol–gel synthesis of lanthanum oxide nanoparticles. *Appl. Phys. A Mater. Sci. Process* **2018**, *124*, 1–11. https://doi.org/10.1007/s00339-018-2246-5.
51. Pérez-Larios, A.; Lopez, R.; Hernández-Gordillo, A.; Tzompantzi, F.; Gómez, R.; Torres-Guerra, L.M. Improved hydrogen production from water splitting using TiO_2–ZnO mixed oxides photocatalysts. *Fuel* **2012**, *100*, 139–143. https://doi.org/10.1016/j.fuel.2012.02.026.
52. Santoso, J.S.; Nusantor, Y.R.; Lestari, W.C.; Choir, A.A. Review: Pengaruh Variasi Suhu Kalsinasi C-TiO_2, Zn-TiO_2, dan La-TiO_2 Terhadap Kristalinitas pada Metode Sol-Gel. Journal of chemistry, 2021, 10, 3. .
53. Zalas, M.; Laniecki, M. Photocatalytic hydrogen generation over lanthanides-doped titania. *Sol. Energy Mater. Sol. Cells* **2005**, *89*, 287–296. https://doi.org/10.1016/j.solmat.2005.02.014.
54. McDevitt, N.T.; Baun, W.L. Infrared absorption study of metal oxides in the low frequency region (700–240 cm^{-1}). *Spectrochim. Acta* **1964**, *20*, 799–808. https://doi.org/10.1016/0371-1951(64)80079-5.
55. Catauro, M.; Tranquillo, E.; Poggetto, G.D.; Pasquali, M.; Dell'Era, A.; Ciprioti, S.V. Influence of the Heat Treatment on the Particles Size and on the Crystalline Phase of TiO2 Synthesized by the Sol-Gel Method. *Materials* **2018**, *11*, 2364. https://doi.org/10.3390/ma11122364.
56. Ruíz-Santoyo, V.; Marañon-Ruiz, V.F.; Romero-Toledo, R.; González Vargas, O.A.; Pérez-Larios, A. Photocatalytic Degradation of Rhodamine B and Methylene Orange Using TiO_2-ZrO_2 as Nanocomposite. *Catalysts* **2021**, *11*, 1035.
57. Nguyen-Phan, T.-D.; Song, M.B.; Kim, E.J.; Shin, E.W. The role of rare earth metals in lanthanide-incorporated mesoporous titania. *Microporous Mesoporous Mater.* **2009**, *119*, 290–298. https://doi.org/10.1016/j.micromeso.2008.10.039.
58. Kumaresan, L.; Prabhu, A.; Palanichamy, M.; Arumugam, E.; Murugesan, V. Synthesis and characterization of Zr^{4+}, La^{3+} and Ce^{3+} doped mesoporous TiO_2: Evaluation of their photocatalytic activity. *J. Hazard. Mater.* **2011**, *186*, 1183–1192. https://doi.org/10.1016/j.jhazmat.2010.11.124.
59. Zhang, Z.; Ni, X.; Yao, K.; Liu, Y.; Sun, Y.; Wang, X.; Huang, W.; Zhang, Y. An electrochemical synthesis of a rare-earth(La3+)-doped ZIF-8 hydroxyapatite composite coating for a Ti/TiO_2 implant material. *New J. Chem.* **2021**, *45*, 6543–6549. https://doi.org/10.1039/d0nj05274d.
60. Briggs, D. Handbool of X Ray Photoelectron Spectroscopy: A Reference Book of Standard Spectra for Identification and Interpretation of XPS Data. In *Handbook of Adhesion*; John Wiley & Sons, Ltd.: Chichester, UK, 2005; pp. 621–622.
61. Thommes, M.; Kaneko, K.; Neimark, A.V.; Olivier, J.P.; Rodriguez-Reinoso, F.; Rouquerol, J.; Sing, K.S.W. Physisorption of gases, with special reference to the evaluation of surface area and pore size distribution (IUPAC Technical Report). *Pure Appl. Chem.* **2015**, *87*, 1051–1069. https://doi.org/10.1515/pac-2014-1117.
62. Walford, E. *Handbook of Inorganic Chemicals*;McGraw Hill 1896, New York.
63. Li, J.P.H.; Zhou, X.; Pang, Y.; Zhu, L.; Vovk, E.I.; Cong, L.; van Bavel, A.P.; Li, S.; Yang, Y. Understanding of binding energy calibration in XPS of lanthanum oxide by in situ treatment. *Phys. Chem. Chem. Phys.* **2019**, *21*, 22351–22358. https://doi.org/10.1039/c9cp04187g.
64. Pérez-Larios, A.; Torres-Ramos, M.; González-Vargas, O.; Rico, J.L.; Zanella, R. Ti–Fe mixed oxides as photocatalysts in the generation of hydrogen under UV-light irradiation. *Int. J. Hydrog. Energy* **2022**. https://doi.org/10.1016/j.ijhydene.2022.04.179.
65. Scoca, D.L.S.; Cemin, F.; Bilmes, S.A.; Figueroa, C.A.; Zanatta, A.R.; Alvarez, F. Role of Rare Earth Elements and Entropy on the Anatase-To-Rutile Phase Transformation of TiO_2 Thin Films Deposited by Ion Beam Sputtering. *ACS Omega* **2020**, *5*, 28027–28036. https://doi.org/10.1021/acsomega.0c03431.
66. Manjumol, K.A.; Smitha, V.S.; Shajesh, P.; Baiju, K.V.; Warrier, K.G.K. Synthesis of lanthanum oxide doped photocatalytic nano titanium oxide through aqueous sol–gel method for titania multifunctional ultrafiltration membrane. *J. Sol-Gel Sci. Technol.* **2010**, *53*, 353–358. https://doi.org/10.1007/s10971-009-2101-4.
67. Eslami, A.; Amini, M.M.; Asadi, A.; Safari, A.A.; Daglioglu, N. Photocatalytic degradation of ibuprofen and naproxen in water over NS-TiO_2 coating on polycarbonate: Process modeling and intermediates identification. *Inorg. Chem. Commun.* **2020**, *115*, 107888. https://doi.org/10.1016/j.inoche.2020.107888.
68. Fan, G.; Zhan, J.; Luo, J.; Zhang, J.; Chen, Z.; You, Y. Photocatalytic degradation of naproxen by a H_2O_2-modified titanate nanomaterial under visible light irradiation. *Catal. Sci. Technol.* **2019**, *9*, 4614–4628. https://doi.org/10.1039/c9cy00965e.
69. Regmi, C.; Kshetri, Y.K.; Pandey, R.P.; Lee, S.W. Visible-light-driven S and W co-doped dendritic BiVO 4 for efficient photocatalytic degradation of naproxen and its mechanistic analysis. *Mol. Catal.* **2018**, *453*, 149–160. https://doi.org/10.1016/j.mcat.2018.05.008.
70. Méndez-Arriaga, F.; Gimenez, J.; Esplugas, S. Photolysis and TiO_2 Photocatalytic Treatment of Naproxen: Degradation, Mineralization, Intermediates and Toxicity. *J. Adv. Oxid. Technol.* **2008**, *11*, 435–444. https://doi.org/10.1515/jaots-2008-0302.
71. Begum, S.; Ahmaruzzaman Biogenic synthesis of SnO2/activated carbon nanocomposite and its application as photocatalyst in the degradation of naproxen. *Appl. Surf. Sci.* **2018**, *449*, 780–789. https://doi.org/10.1016/j.apsusc.2018.02.069.